Role of Dopants in Long-Range Charge Carrier Transport for p-Type and n-Type Graphene Transparent Conducting Thin Films

Justin B. Bult, Ryan Crisp, Craig L. Perkins, and Jeffrey L. Blackburn*

National Renewable Energy Laboratory, 16253 Denver West Parkway, Golden, Colorado 80401, United States

ABSTRACT Monolayer to few-layer graphene thin films have several attractive properties such as high transparency, exceptional electronic transport, mechanical durability, and environmental stability, which are required in transparent conducting electrodes (TCs). The successful incorporation of graphene TCs into demanding applications such as thin film photovoltaics requires a detailed understanding of the factors controlling long-range charge transport. In this study, we use spectroscopic and electrical transport measurements to provide a self-consistent understanding of the macroscopic (centimeter, many-grain scale) transport properties of chemically doped p-type and n-type graphene TCs. We demonstrate the first large-area n-type graphene TCs through the use of hydrazine or polyethyleneimine as dopants. The n-type graphene TCs utilizing PEI, either as the sole dopant or as an overcoat, have good stability in air compared to TCs only doped with hydrazine. We demonstrate a shift in Fermi energy of well over 1 V between the n- and p-type graphene TCs and a sheet resistance of ~50 Ω/sq at 89% visible transmittance. The carrier density is increased by 2 orders of magnitude in heavily doped graphene TCs, while the mobility is reduced by a factor of ~7 due to charged impurity scattering. Temperature-dependent measurements demonstrate that the molecular dopants also help to suppress processes associated with carrier localization that may limit the potential of intrinsic graphene TCs. These results suggest that properly doped graphene TCs may be well-suited as anodes or cathodes for a variety of opto-electronic applications.

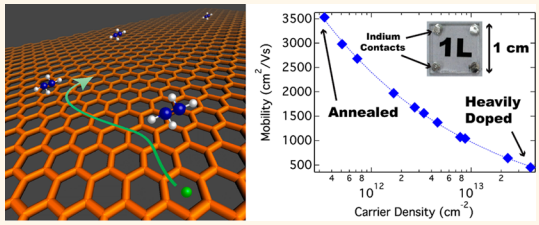

KEYWORDS: graphene · transparent conductor · charged impurity · scattering · photovoltaics · conductivity · mobility · transport · temperature-dependent

Transparent conducting electrodes (TCs) are integral parts of numerous important applications, such as photovoltaics (PV), portable electronics, and touch screens. The two most important performance metrics for TCs are the transmittance (T) of incident photons and the sheet resistance, R_s, which defines the resistance to two-dimensional charge carrier transport. Most solar cells utilize transparent conducting oxides (TCOs) that typically transmit at least 87% of the visible solar flux to the PV active layer and possess R_s values in the 10−100 Ω/sq range.[1] The majority of these TCOs, such as tin-doped indium oxide (ITO), fluorine-doped tin oxide (FTO), and cadmium-doped tin oxide (cadmium stannate), are n-type conductors with high carrier concentrations (>10^{20} cm^{-3}) arising from the introduction of atomic impurity dopants.[2,3] These high carrier concentrations limit the mobility *via* ionized impurity scattering[4] and also lead to a large free carrier absorbance onset in the near-infrared, dramatically reducing the transmittance of photons with wavelengths greater than ~1000 nm.

A variety of nanostructured transparent conducting thin films has emerged in recent years in an effort to find cost-effective alternatives to TCOs,[5] including single-walled carbon nanotube thin films,[6−8] conducting polymer films,[9] metallic nanowire networks,[10,11] and graphene thin films.[12−15] Graphene thin films are both highly transparent and conductive, can be produced over large areas, and can be transferred to a variety of substrates *via* roll-to-roll techniques, making them attractive candidates for opto-electronic applications that require TCs.[16] Graphene TCs can also potentially fill niches that traditional TCOs are not well-suited for. For example, graphene

* Address correspondence to jeffrey.blackburn@nrel.gov.

Received for review May 27, 2013 and accepted July 16, 2013.

Published online July 16, 2013
10.1021/nn402673z

TCs maintain high conductivity on flexible substrates after repeated bending,[17] the semimetallic band structure of graphene affords widely variable work functions based on a continuously tunable Fermi energy,[18] and the relatively flat absorbance of graphene TCs makes them highly transparent over the entire range of the solar spectrum. These attributes open up numerous opportunities for graphene TCs as both cathodes and anodes in applications such as PV, especially for flexible thin film solar cells and devices that require efficient capture of near-infrared photons (*e.g.*, tandem cells).[19]

Despite the recognized potential for graphene TCs in opto-electronic applications, the majority of detailed transport studies have focused on the microscopic (*i.e.*, single- to few-grain) transport properties of graphene. To realize the full potential of large-area graphene thin films in areas such as PV, there is a clear need for more studies exploring the macroscopic transport properties over length scales of centimeters and beyond and how these macroscopic properties may affect the performance of graphene TCs in devices. For example, what roles do molecular charge transfer dopants (an analogue to atomic impurity dopants in TCOs) play in determining charge carrier density (n_i), mobility (μ), and work function (Φ) at the macroscopic level? What roles do static potential fluctuations, grain boundaries, and defects play in carrier localization and scattering? Can systematic studies help to explain the large variability in values reported for T and R_s in the literature for large-area graphene thin films? Finally, how tunable and how stable with respect to various ambient conditions are n_i, μ, and Φ for molecular charge transfer dopants?

Here we describe a detailed study of long-range electron and hole transport in undoped and chemically doped graphene TCs. We first demonstrate large-area *n-type graphene TCs*, achieved by doping with hydrazine or polyethyleneimine,[7] that compliment the much more heavily studied p-type graphene TCs. A variety of macroscopic, spectroscopic, and electrical characterization tools are used to attain a self-consistent quantitative understanding of the changes in sheet resistance, carrier density, mobility, and Fermi energy induced by representative n- and p-type dopants. Temperature-dependent transport measurements are then used to understand the mechanisms underlying long-range charge transport both close to and far away from the Dirac point.

The results obtained here indicate that molecular dopants are needed to obtain graphene TCs with low enough R_s to be useful for demanding applications such as PV, with T and R_s values of ~89% and 50 Ω/sq achieved for four-layer n- or p-type graphene TCs. These molecular dopants are needed to provide appreciable carrier density for high conductivity but also serve to raise the Fermi energy above the magnitude of potential fluctuations induced by static disorder that lead to localized (thermally activated) carriers. We demonstrate that although the mobility of doped graphene TCs is limited by charged impurity scattering, the high carrier density injected by the dopants offsets this reduction in mobility, affording a reduction in sheet resistance of over an order of magnitude relative to nearly intrinsic TCs. Finally, we show that our n- and p-type films enable a continuously tunable Fermi energy over a range of >1 V.

RESULTS

Transmittance and Sheet Resistance. Figure 1a displays the transmittance of single-layer to four-layer (1L to 4L) graphene films produced by subsequent transfers of monolayer graphene to glass substrates. The inset to Figure 1 compares the measured transmittance to the expected transmittance for each film $(100 - (2.3 \times L))$,[20] where L = the number of layers. The measured 1L film transmittance coincides with that expected from the graphene fine structure constant, whereas the measured values deviate as successive layers are transferred, and the 4L film is ~2% less transparent than expected. This deviation has been observed in previous studies on PMMA-transferred graphene thin films[21−23] and was attributed to residues incurred in the transfer process. In our case, the reduced transparency likely results from a combination of transfer residues and an

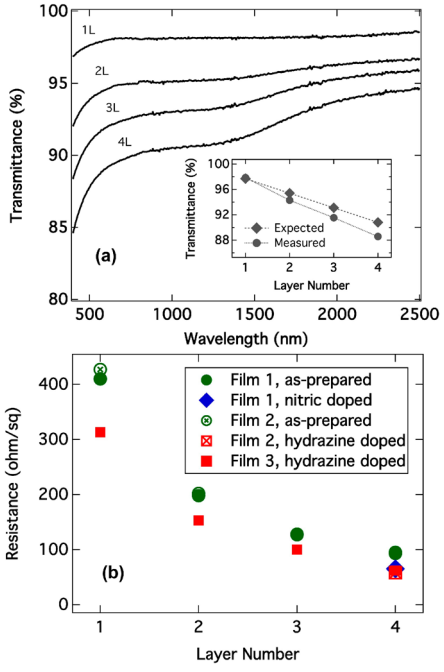

Figure 1. (a) Transmittance of graphene sheets with 1−4 layers. Inset shows the expected and observed transmittance at 550 nm for each layer number. (b) Sheet resistance as a function of layer number for graphene sheets, as measured by four-point probe. Film 1 was doped with 4 M nitric acid after four transfers, and film 2 was doped with 4 M hydrazine after four transfers. Film 3 was doped with hydrazine for each successive transfer.

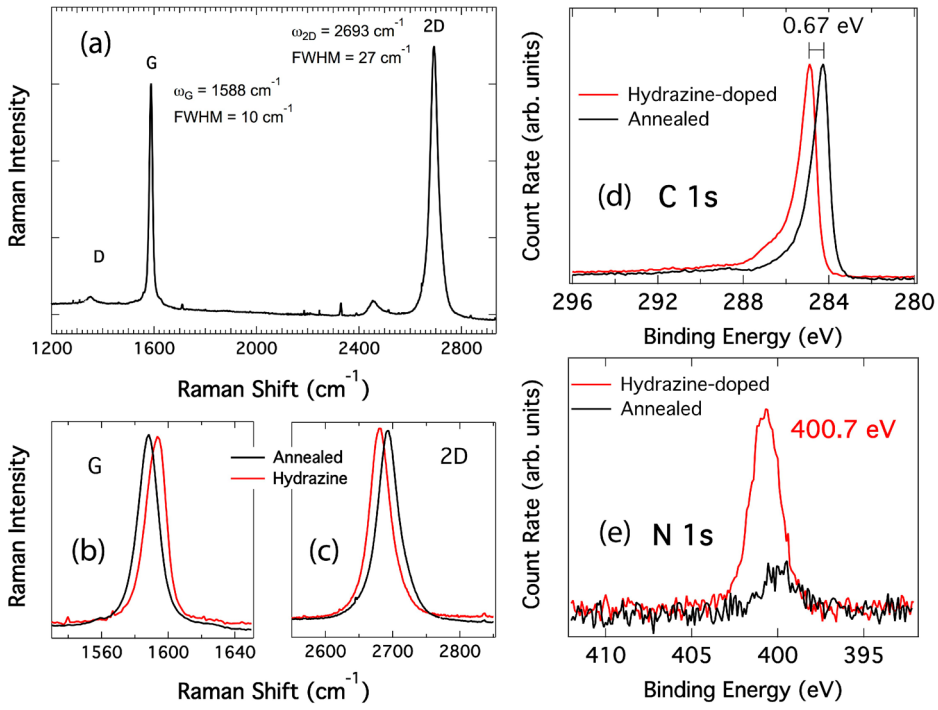

Figure 2. Spectroscopic confirmation of n-type doping by hydrazine (all panels show 1L graphene). (a) Full Raman spectrum for as-prepared graphene (undoped). (b) G band Raman shifts for hydrazine-doped and annealed graphene TCs. (c) 2D Raman shifts for hydrazine-doped and annealed graphene TCs. (d) C 1s XPS spectra for annealed and hydrazine-doped graphene TCs. (e) N 1s XPS spectra for annealed and hydrazine-doped graphene TCs.

appreciable density of multilayer nucleation centers that are visible in Raman mapping measurements (Supporting Information, Figure S1).

Figure 1b displays the measured sheet resistance (R_s) values of 1L−4L graphene films, either as-prepared or intentionally doped (nitric acid or hydrazine), as measured by four-point probe. The as-prepared films vary from ∼400 Ω/sq (1L) to ∼96 Ω/sq (4L), values that are slightly higher (∼1.4−1.9×) than the best R_s values reported recently for graphene TCs transferred by heat transfer tape[12] but significantly lower (∼3−5×) than several recent reports for graphene TCs transferred by a PMMA process.[14,21] Doping with either nitric acid or hydrazine significantly lowers R_s of the graphene films. For both nitric acid and hydrazine, doping a 4L film reduces R_s from ∼96 to ∼56 Ω/sq, suggesting they are equally effective at doping graphene, as was recently observed for SWCNT transparent conductors.[7]

Spectroscopic Confirmation of n-Type Doping By Hydrazine. Nitric acid is well-known to produce p-type graphene TCs, but n-type TCs are significantly less studied.[7,24] Since the sheet resistance of the graphene films gives no indication of carrier type, we performed a series of experiments to validate the carrier type and Fermi level shift induced by hydrazine doping. The vibrational modes of graphene are sensitive to the charge density in the extended π electron network and are frequently used as a probe of the magnitude and direction of charge transfer.[25] Figure 2 shows Raman spectra, taken at 532 nm with a spot size of ∼250 μm, for the annealed and hydrazine-doped films. Due to the large area of the beam, these Raman measurements capture the scattering from multiple grains (average grain size is ∼20 μm; see Supporting Information, Figure S2) and also contain contributions from Raman scattering at grain boundaries. Figure 2a shows the full spectrum of the as-prepared sample and is dominated by the tangential mode (G band) at 1588 cm^{-1} and the second-order 2D mode at 2693 cm^{-1}. The width and intensity ratios for the G and 2D modes are representative of high-quality monolayer graphene when measured over large areas (*i.e.*, with a large spot size). The disorder peak, or D band, is also visible at ∼1340 cm^{-1}. These graphene samples have a consistently low I_D/I_G intensity ratio of ∼0.02, indicating a relatively low defect density.[26,27]

Figure 2b,c displays the spectral shifts induced in the G and 2D modes, respectively, upon doping a graphene film with hydrazine. A ∼5 cm^{-1} blue shift of the G band accompanies a ∼14 cm^{-1} red shift of the 2D band for the hydrazine-doped film relative to an annealed (undoped) sample. These shifts can be understood within the framework of the adiabatic and nonadiabatic contributions of doping on the Raman spectrum.[25] In the adiabatic case, electron injection into or removal from the π network induces a slight expansion or contraction of the lattice, respectively. The lattice expansion (contraction) in turn leads to a red shift (blue shift) for the n-type (p-type) graphene. The adiabatic term is the only contribution to the

higher energy 2D mode,[25] so the ~14 cm^{-1} red shift of the 2D mode for the hydrazine-treated sample suggests that hydrazine injects a significant density of *electrons* into the graphene film, producing an n-type transparent conductor. Electron–phonon coupling to the lower energy G mode induces an additional nonadiabatic contribution. In this case, phonon renormalization occurs as a result of the coupling of LO phonons to low-energy electronic excitations, and a blue shift of the G band is expected for both p-type and n-type doping. Thus, the ~5 cm^{-1} blue shift for the hydrazine-doped sample (relative to the annealed film) indicates that the Fermi energy has been shifted significantly away from the Dirac point, while the red shift of the 2D band confirms that the *direction* of the Fermi energy shift is toward vacuum (n-type doping).

To validate the Raman analysis for hydrazine-doped graphene TCs, we performed X-ray photoelectron spectroscopy (XPS) to probe the composition and doping-induced valence band shifts in the annealed and hydrazine-doped samples. Figure 2c shows the C 1s XPS spectra for these two samples and illustrates a large shift of 670 meV to higher binding energy for the hydrazine-doped sample relative to the annealed sample. Since the binding energy in the XPS measurement is referenced to the Fermi energy, and assuming a rigid shift of the valence band edge with the core levels, the higher binding energy for the hydrazine-doped sample indicates that the Fermi energy has been moved 670 meV closer to vacuum by hydrazine adsorption.[7] The linear band structure of graphene allows for a relatively straightforward correlation of the Fermi energy (E_F) with the carrier density, through the relationship

$$E_F(n_i) = \hbar v_F \sqrt{\pi n_i} \quad (1)$$

where $v_F = 1.1 \times 10^6$ ms^{-1} is the Fermi velocity and $\hbar = 1.05457 \times 10^{-34}$ J·s. Using eq 1, the 670 meV change in Fermi energy (ΔE_F) measured by XPS demonstrates that the adsorbed hydrazine molecules inject an electron density of ~2×10^{13} cm^{-2}.

The N 1s XPS spectra, shown in Figure 2d, provide information on the nitrogen-containing species physisorbed on the surface of the hydrazine-doped and annealed samples. The annealed sample contains a small N signal at 400 eV, which is in the region expected for amines (399–401 eV).[28] This signal most likely originates from residual ammonium persulfate that persists even after annealing (see also Supporting Information, Figure S4). The hydrazine-doped sample shows a much stronger N 1s signal at 400.7 eV, which arises from the adsorbed N_2H_4 molecules. The integrated area underneath the nitrogen and carbon regions suggests that the graphene surface is covered with approximately 56 N atoms (or 28 N_2H_4 molecules) for every 1000 C atoms, or a coverage of ~1×10^{16} cm^{-2}. Using the injected carrier density of ~2×10^{13} cm^{-2} estimated by the shift in C 1s binding energy, this translates to an injection of ~0.002 electrons per hydrazine molecule. If we assume that there may still be some contribution of the ammonium peak observed for the annealed sample in the hydrazine-doped N 1s spectrum, this value increases slightly to ~0.0024 e^-/molecule.

TABLE 1. Transport Properties of 1L Graphene Films As Measured by the Hall Technique

	R_s (Ω/sq)	HC (m^2/C)	μ (cm^2 V^{-1} s^{-1})	n_i (cm^{-2})	E_F (meV)
as-prepared	674	+129	1910	$+4.84 \times 10^{12}$	+282
annealed	4262	+1240	2920	$+5.02 \times 10^{11}$	+91
nitric-doped	416	+26.8	643	$+2.33 \times 10^{13}$	+580
hydrazine-doped	517	−94.6	1830	-6.60×10^{12}	−330
hydrazine + PEI	380	−32.2	848	-1.94×10^{13}	−565
PEI-doped	397	−38	957	-1.64×10^{13}	−520

Room Temperature Transport Measurements. *Room Temperature Hall Measurements.* To provide a more quantitative analysis of the transport properties for these films, we turn to Hall measurements on large-area (1 × 1 cm) graphene TCs. Table 1 displays the sheet resistance (R_s), Hall coefficient (HC), mobility (μ), and carrier density (n_i), as extracted by Hall measurements for 1L graphene TCs subjected to different treatments. We note that the samples need to be exposed to air for at least 1 min before pulling vacuum in the Hall setup. Our previous measurements on SWCNT TCs suggested that the n-type conductivity of hydrazine-doped films can degrade in air, but that this degradation could be hindered by a thin overcoat of polyethyleneimine (PEI).[7] Therefore, we studied three samples doped with amine-containing moieties: a hydrazine-doped sample, a PEI-doped sample, and a hydrazine-doped sample with a thin overcoat of PEI.

The signs of the Hall coefficients and carrier densities are all positive for the as-prepared, annealed, and nitric-doped samples, indicating that holes are the majority carriers for all of these films. In contrast, the signs of HC and n_i are negative for the samples doped with hydrazine and/or PEI, confirming they are n-type TCs. The sample doped only with hydrazine suffered a significant increase in sheet resistance and decrease in electron density over the short duration of air exposure (~1 min) necessary for transfer from the glovebox to the vacuum environment of the Hall system. The highest electron density and lowest sheet resistance was found for the hydrazine-doped sample that was overcoated with PEI, although the sample doped only with PEI performed nearly as well. The mechanisms underlying the degradation of n-type transport will be discussed in the following section. The as-prepared TC has a reasonably high hole density of ~4.84×10^{12} cm^{-2}, which is lowered by an order of magnitude to 5.02×10^{11} cm^{-2} upon annealing at 150 °C.

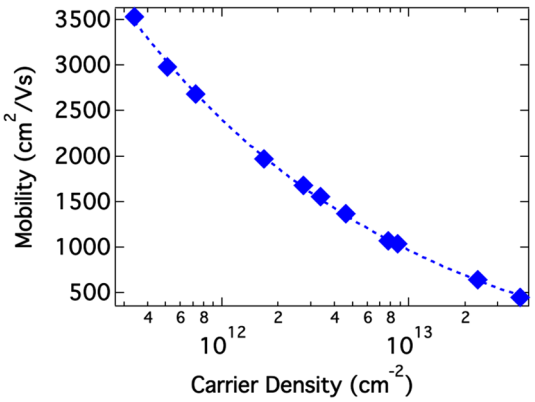

Figure 3. Hall mobility for a 1L nitric-doped p-type graphene TC in which the carrier concentration is modulated by thermal desorption of nitric acid from an initially heavily doped film. Points are experimental data, and blue dashed line is fit (see text).

Interestingly, the sheet resistance of the annealed sample is nearly an order of magnitude higher (4262 Ω/sq) than the as-prepared sample (674 Ω/sq). R_s for the annealed TC is also significantly higher than R_s values typically reported for 1L graphene TCs,[12,14,21] suggesting that the majority of studies probe as-prepared graphene TCs that are significantly doped from the acidic etchants used to remove the copper substrate. The hydrazine-doped and nitric-doped TCs have nearly identical electron and hole densities, respectively, of $\sim 2 \times 10^{13}$ cm^{-2}, consistent with their similar R_s values.

For all samples in Table 1, the mobility appears to vary inversely with the magnitude of the carrier density, indicating scattering processes correlated with physisorbed dopants. To investigate this correlation more systematically, we doped a 1L graphene TC p-type with nitric acid and performed Hall measurements on this sample at various doping levels. The doping levels, and thus E_F and n_h, were controlled by partial thermal desorption of the adsorbed nitric acid. Figure 3 illustrates that the room temperature hole mobility decreases with carrier concentration over 2 orders of magnitude, in this case following a dependence of $\mu \propto 1/n^x$, where $x \approx 0.62$ (dashed fit line). This anticorrelation between mobility and carrier density is an unambiguous signature of charged impurity scattering,[29] in which a charge carrier is scattered by the Coulomb potential created by the adsorbed dopant. Interestingly, some studies on micromechanically exfoliated graphene have suggested a negligible reduction in mobility *via* charged impurity scattering associated with either the substrate[30] or even with intentionally adsorbed dopants,[31] up to carrier densities well above $N = 10^{12}$ cm^{-2}. However, Figure 3 demonstrates that for large-area CVD-grown graphene, the presence of adsorbed molecular dopants leads to a significant reduction in mobility over a wide range of carrier densities.

Equation 1 was used to estimate the Fermi energy (relative to the Dirac point, where $E_F \equiv 0$), based on the free carrier concentrations (n_i) extracted from the Hall measurements, and this calculated Fermi energy is displayed in the last column of Table 1. Because of adventitious doping from the copper etching process, the Fermi energy is nearly 300 meV positive of the Dirac point for the as-prepared sample. The carrier density and sheet resistance values for these as-prepared films vary significantly, both from batch to batch and with time, due to lack of control over the doping imparted by the transfer process and ambient conditions, as well as time-dependent dedoping of the films. Annealing at 150 °C moves the Fermi energy to within ~90 meV of the Dirac point but still does not return the graphene to fully intrinsic. It is likely that this nonzero Fermi energy results from unavoidable interactions with the substrate, as surface oxides on glass, quartz, and silicon (*e.g.*, thermal oxides) are known to dope graphene p-type and also break up the graphene potential landscape into "electron–hole puddles".[32,33] When intentionally doped with either hydrazine or nitric acid, the Fermi energy is pushed over 550 meV in either direction due to the large density ($\sim 2 \times 10^{13}$ cm^{-2}) of injected carriers. It is important to point out that carrier density and Fermi energy shift obtained by Hall measurements is nearly identical to the values obtained by XPS. The XPS measurements indicate a shift in Fermi energy of 670 meV toward vacuum for the hydrazine-doped TC relative to the annealed TC. Similarly, the total Fermi energy shift estimated by the Hall measurements for the same samples is 656 meV. This agreement provides a useful confirmation of the quantitative metrics obtained by the Hall measurements. This Fermi energy shift can also be related to the work function of the graphene TCs, an important metric for using the TCs in PV applications. If we assume a work function of 4.6 eV for 1L graphene,[34] these Fermi energy shifts correspond to a fully tunable range of ~4.0 to 5.1 eV for the work function of our doped graphene TCs. However, we note that this estimated range does not take into account any work function shifts resulting from surface dipoles, meaning the actual range could be slightly different. Importantly, this wide range matches well with the values needed for a variety of PV applications, meaning they can be used as highly conductive *anodes or cathodes* in thin film PV applications.[35–37]

Compensation of n-Type Graphene TCs. The Hall measurement of the hydrazine-doped TC demonstrate that n-type conductivity degrades upon exposure to air, but that high electron densities can be maintained in graphene TCs doped (or coated) with PEI. Possible degradation mechanisms include the irreversible reaction of hydrazine with oxygen to produce nitrogen and water and the potentially reversible compensation of electrons by physisorption of oxygen and/or water

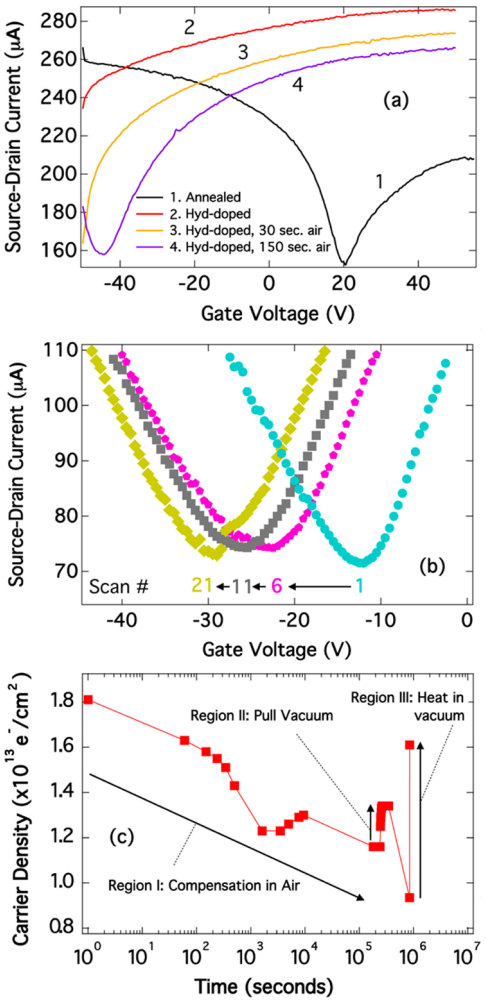

Figure 4. (a) Bottom-gated FET transfer curves of an annealed 1L graphene TC (1) and a hydrazine-doped n-type graphene TC subjected to 0−150 s of air exposure (2−4). The channel length was 25 μm. (b) FET transfer curves for a 1L hydrazine-doped n-type graphene TC that was exposed to air for 70 min and then returned to the glovebox for measurement. The FET was subjected to a series of scans, resulting in a systematic shift of V_m to more negative gate voltages. The scan number is listed at the bottom underneath each corresponding transfer curve. The channel length was 50 μm. (c) Electron density, as measured by Hall, for a hydrazine-doped, PEI-overcoated n-type 1L graphene TC exposed to air at t = 0.

molecules. We performed two experiments to probe the mechanism of n-type degradation of our graphene TCs. In one experiment, we fabricated bottom-gated (and bottom-contacted) hydrazine-doped field effect transistors (FETs) that we characterized in an inert glovebox. In a gate voltage sweep (constant source−drain current), the minimum gate voltage (V_m) is a good qualitative indicator of Fermi energy and carrier type. $V_m > 0$ indicates p-type graphene, $V_m < 0$ indicating n-type graphene, while $V_m = 0$ indicates intrinsic graphene. Figure 4a demonstrates that V_m for the annealed graphene TC is ∼20 V, indicative of residual p-type doping, consistent with the Hall measurements. Doping the film with hydrazine induces a shift in V_m to a very large negative gate voltage that is well outside our measurement range. This large shift implies that hydrazine has doped the film strongly n-type, further confirming the conclusions reached by Raman, XPS, and Hall measurements.

Exposing the n-type FET to air for 30 and 150 s induces a shift of V_m toward zero, indicating that air exposure lowers the Fermi energy, with longer exposures resulting in Fermi energies closer to the Dirac point. However, upon cycling our air-exposed FETs, we observed an interesting dynamic process, shown in Figure 4b, for a hydrazine-doped film that was exposed to air for 70 min. Upon cycling this film, V_m shifted from −12 to −29 V, indicating that successive sweeps of the gate voltage raised the Fermi energy back away from the Dirac point toward more negative potentials. This behavior is consistent with at least some portion of the degradation of n-type behavior upon air exposure being reversible upon applying a large bias to the n-type TC. The reversibility of this degradation suggests that physisorbed ambient molecules compensate the hydrazine-injected electrons, but at least some portion of these molecules can be subsequently desorbed by the current-induced increase in the sample temperature.

To probe this phenomenon in more detail, and also to attempt to slow the compensation process, we performed a time-dependent Hall transport study on a hydrazine-doped, PEI-coated graphene TC (Figure 4c). There are three important regions to point out. The first is region I, which represents the first ∼2.5 days of air exposure. During this time period, the free carrier density slowly (and nonlinearly) decreases from 1.8×10^{13} to 1.16×10^{13} e$^-$/cm^2. At this point, we pulled vacuum on the sample (region II) and observed a rapid increase of the free carrier density back to 1.31×10^{13} e$^-$/cm^2. After this vacuum exposure, the sample was returned to air, at which point the carrier density further decreased. The sample was then returned to vacuum and subjected to a 350 K heat treatment for 5 min (region III). This heat treatment increased the free carrier density to 1.61×10^{13} e$^-$/cm^2, nearly back to the original value before any air exposure. These results clearly demonstrate a compensation of free electrons in the n-type graphene TC by either water, oxygen molecules, or both, and that this compensation can be reversed by a mild heat treatment in vacuum. Additionally, the PEI overcoating provides a reasonable amount of air stability to the n-type graphene TC, as R_s only increased by ∼20% over the course of 5 days and the TC remained strongly n-type. In comparison, the electron density in a similar hydrazine-doped 1L film that did not receive an overcoat of PEI was already reduced to $\sim 6 \times 10^{12}$ cm^{-2} after ∼1 min and decreased to $<10^{12}$ cm^{-2} within 24 h (Supporting Information Figure S6).

Temperature-Dependent Transport. The temperature dependence of electrical transport can provide

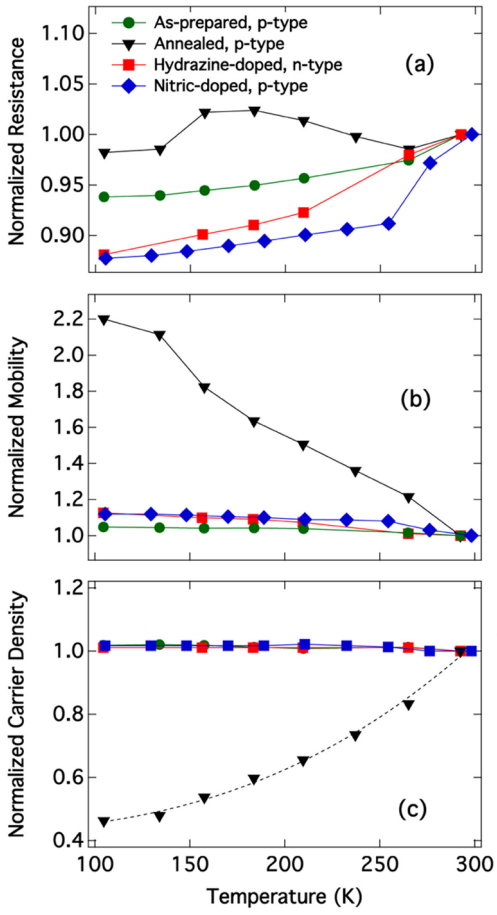

Figure 5. Temperature-dependent Hall transport measurements for 1L graphene TCs. (a) Sheet resistance, (b) carrier mobility, and (c) carrier density of as-prepared (p-type), hydrazine-doped (n-type), and annealed samples. The solid lines connecting points are a guide for the eye. The dashed line in (c) is a quadratic fit to the carrier density dependence, as suggested by eq 2.

detailed insight into the scattering mechanisms controlling long-range transport in graphene.[38,39] Although a number of temperature-dependent transport measurements have been reported for isolated grains of graphene, either in contact with a substrate or suspended above trenches, the literature is sparse for graphene films with areas large enough to be relevant to transparent conducting electrodes. Figure 5a shows the temperature-dependent R_S of three representative graphene TCs: as-prepared, annealed, and hydrazine-doped. There is an obvious positive temperature coefficient for the resistance of the as-prepared and intentionally doped (nitric and hydrazine) films, an indication of metallic-like conductivity. In contrast, the annealed film has a very weak temperature coefficient, with resistance values that oscillate around the room temperature value. The temperature dependences of the mobility and carrier density, plotted in Figures 4b,c, help to explain these trends. For both the as-prepared and the intentionally doped films, the mobility is weakly temperature-dependent, with a negative temperature coefficient, and the carrier density is temperature-independent. For both of these films, the temperature-dependent carrier mobility produces the positive temperature coefficient for the resistance observed in Figure 5a.

In contrast, for the annealed film, both the carrier mobility and density are very strongly temperature-dependent and have opposite temperature coefficients. Over the measured temperature range, the mobility decreases by a factor of ~2.2, while the carrier density increases by a factor of ~2.2. These opposing, and nearly equivalent, temperature coefficients roughly cancel each other out and explain the weak temperature dependence of the resistance for the annealed film. The fact that the mobility and carrier density have slightly different derivatives for their temperature dependence explains the interesting oscillations about $R/R_{RT} = 1$. This "hump" in the temperature-dependent R_s was found to be reproducible over many samples, although its physical origin remains unclear.

To understand the trends observed in Figure 5, we turn to some recent theoretical work. The strongly activated carrier density (Figure 5c) of the annealed film is certainly the most striking trend and one that has been predicted for graphene films at low carrier density (*e.g.*, $<1 \times 10^{12}$ cm^{-2}) by Li *et al.*[40] Near the charge-neutral point, that is, at low carrier densities, charged impurities in the substrate break up the potential landscape of monolayer graphene into a series of electron−hole puddles. These electron−hole puddles can be viewed as local potential fluctuations with magnitude V and standard deviation s that modify the density of states near the charge-neutrality point. The band tails created in the density of states lead to a nonzero carrier density at $T = 0$, n_0, and an activated carrier density at finite temperatures, $n_e(T)$, that is described by the equation

$$n_e(T) = n_0\left[1 + \frac{\pi^2}{3}\left(\frac{k_B T}{s}\right)^2\right] \quad (2)$$

where s is the standard deviation (or strength) of the potential fluctuation, and k_B is the Boltzmann constant.[40] The carrier concentration in the band tails, n_0, is related to the magnitude of the disorder by

$$n_0 = D_1\frac{s^2}{4} \quad (3)$$

where D_1 describes the density of states for graphene's linear bands, and $D_1 = 1.5 \times 10^8$ cm^{-2}/meV^2.[40]

Equations 2 and 3 are valid for graphene samples that are not intentionally doped, that is, are near the charge-neutrality point, where the main source of carriers is the potential fluctuations arising from static disorder. As such, our annealed film could be expected to show a quadratic dependence of carrier density on temperature if the main source of this activated

behavior arises from the influence of electron−hole puddles. Fitting eq 2 to the data (dashed black line, Figure 4c) demonstrates that the annealed film does exhibit a quadratic dependence of carrier density on T and yields values of $n_0 = 2.2 \times 10^{11}$ cm^{-2} and $s = 77$ meV.

An obvious result from Figure 5c is that the temperature dependence of the carrier density is dramatically suppressed by molecular charge transfer dopants that are adsorbed either intentionally or unintentionally. Thus, Figure 5 demonstrates another important role that molecular dopants play in the long-range transport for graphene transparent conductors beyond simply increasing the carrier density. *The molecular dopants increase the magnitude of the Fermi energy such that E_F exceeds the magnitude of the static potential fluctuations that cause localization of carriers near the Dirac point.* This suppression of the activated behavior from adsorbed dopants occurs because the activated portion of the carrier density at *finite doping* depends on the relative energies of the Fermi energy, thermal energy, and magnitude of the potential fluctuations (s) through a temperature-dependent term (T^2/T_F^2, where $T_F = E_F/k_B$) and a term that scales with (s/E_F).[40] Both terms are strongly suppressed when E_F is raised well above s, which in turn suppresses the activated behavior for carrier density.

Figure 5b illustrates a strong temperature dependence for the mobility of the annealed sample. All three samples show a negative temperature coefficient for mobility, but the dependence is significantly stronger for the annealed sample. A negative temperature coefficient for mobility is in line with scattering due to phonons, point defects, and screened Coulomb impurities.[38−40] A number of studies have demonstrated the importance of phonon scattering to the temperature-dependent mobility in graphene near the charge-neutrality point, with contributions from both acoustic phonons in graphene and polar optical phonons of SiO_2.[38,39] Interestingly, this negative temperature coefficient is again strongly suppressed in the doped samples, but it is important to remember that the observed mobility, μ_{obs}, must take into account all scattering processes, through Matthiessin's rule:

$$\frac{1}{\mu_{obs}} = \sum \frac{1}{\mu_i} \qquad (4)$$

where μ_i represents the mobility contribution of a particular individual process. As shown in Figure 3, chemical doping of the graphene TCs reduces the mobility *via* charged impurity scattering, which is expected to give rise to a *positive* temperature coefficient for mobility.[4] Thus, chemical doping suppresses the *negative* temperature coefficient of mobility observed for the annealed sample[38,39] through a counteracting *positive* coefficient related to charged impurity scattering. The fact that the overall temperature coefficient remains weakly negative implies that the positive temperature coefficient induced by charged impurity scattering is slightly outweighed by the negative coefficients induced by phonon scattering.[37,38] Indeed, in most doped semiconductors, the positive temperature coefficient of ionized impurity scattering can only be observed at temperatures well below 100 K where phonon effects are less prominent.[4]

DISCUSSION AND CONCLUSIONS

It is useful to briefly discuss the relevance of these results with regard to the use of graphene TCs in demanding electronic applications such as photovoltaics, as well as some important aspects for future studies. We have previously studied the performance of single-walled carbon nanotube TCs in detail,[6,8,41] and there are some useful comparisons to be made. First, the 4L graphene TCs demonstrated in this study are ∼15% more transparent in the visible and infrared than SWCNT TCs with comparable R_s (∼50 Ω/sq).[7,8] Additionally, temperature-dependent resistance measurements on SWCNT TCs demonstrate an overall insulating behavior (negative temperature coefficient for R_s), even for films prepared from ∼100% metallic SWCNTs.[6,41] This activated conductivity points to a dominant influence of the resistance of tube−tube junctions, a potentially limiting factor for the implementation of SWCNT TCs. In contrast, the positive temperature coefficients observed for graphene TCs (overall metallic behavior) imply a weaker influence of grain boundary scattering on the ultimate performance of graphene TCs. Nevertheless, grain boundary scattering should certainly be important and warrants future studies.

Another important difference between the SWCNT and graphene TCs is the effectiveness of PEI as an n-type dopant. We found for SWCNTs that PEI doping produced conducting films that were around three times as resistive as hydrazine-doped films. In contrast, PEI-doped graphene films perform nearly identically to hydrazine-doped films in terms of sheet resistance and electron density. This difference likely stems from steric problems associated with intercalating the PEI polymer into a porous SWCNT network that are not encountered for flat graphene films with totally accessible surfaces. The ability to tune the work function of graphene TCs, especially toward lower work functions as in our hydrazine- and PEI-doped TCs, is an important capability. For example, in organic photovoltaics, the work function of the electrode determines the built-in electric field needed to optimize charge extraction.[37] Additionally, unique solar cell architectures, such as inverted[36] or tandem devices,[42] can be optimized with tunable, low work function transparent negative electrodes such as the n-type graphene TCs demonstrated here.

Another factor that is likely significant for long-range transport behavior in graphene TCs that we did not

touch upon in this study is the *transfer process*. Nearly all of the studies exploring the properties of graphene TCs have utilized a poly(methyl methacrylate) (PMMA) stamp transfer method to transfer the graphene to a substrate of choice.[21] Our study is one of only a few to utilize heat transfer tape for graphene transfer, and the TC performances demonstrated here are fairly close in performance to the seminal work of Bae *et al.*[12] The influence of the transfer method is a large unknown, but it is likely quite important in terms of maintaining an intact graphene sheet (*e.g.*, physical tearing) and minimizing residues that may reduce mobility/conductivity (see also Supporting Information, Figures S1−S3). At the very least, the heat transfer tape method is industrially relevant and should be studied in further detail. Similarly, the *substrate* to which the graphene is transferred influences the resulting long-range transport properties. We have found R_s values approximately 20% lower for graphene samples transferred to flexible substrates such as PET or PEN. *Thus, graphene TCs represent a rare class of TCs that are both more conductive on flexible substrates relative to rigid substrates and retain their high conductivities on flexible substrates subjected to repeated bending cycles.* Such TCs are highly desirable for applications such as flexible touch screens and thin film flexible PV.

Ultimately, our results emphasize the important roles that charge transfer dopants play in the performance of graphene TCs. Although p- and n-type chemical dopants significantly reduce the carrier mobility, by as much as a factor of 7 for a heavily doped film, they are ultimately necessary to reduce the sheet resistance into a reasonable range for applications (*e.g.*, <100 Ω/sq) since they increase the *carrier density* by ∼2 orders of magnitude. The high density of carriers injected by these dopants also serves to raise the Fermi level well above the potential fluctuations induced by static disorder that lead to strongly activated carrier density for intrinsic, undoped graphene TCs. The combination of these effects implies that some form of chemical doping is likely necessary for graphene TCs to achieve performance metrics that are suitable for incorporation into highly demanding applications such as PV.[5] We note that other approaches have also been recently developed to circumvent the need for chemical dopants, such as hybrid graphene TCs incorporating metallic nanowires.[13] Such approaches are very promising but may also have some drawbacks, including cost (*e.g.*, for silver nanowires) and stability (*e.g.*, oxidation of silver or copper nanowires). It is important to note that chemical doping suffers its own inherent drawbacks, primarily related to environmental stability. For example, our measurements demonstrate that electrons injected by hydrazine and/or PEI in n-type graphene TCs are compensated in ambient conditions. However, this compensation is at least partially reversible by heat/vacuum treatments and is severely slowed by the use of PEI as either the sole dopant or as a thin overcoat. These results suggest that these low work function n-type graphene TCs may actually be quite stable once incorporated into full devices, such as organic photovoltaic cells, where the active layer and/or encapsulant can protect against compensation. Some p-type dopants such as nitric acid are quite thermally labile, a property we utilize to study a full range of doping-modulated carrier concentrations in Figure 3. However, the ease with which nitric acid desorbs is detrimental to long-term stability in devices, and more stable alternatives are needed. Previous studies on SWCNT TCs suggest that species such as thionyl chloride[41] and triethyloxonium hexachloroantimonate[43] could be viable alternatives for more thermally stable p-type graphene TCs.

METHODS

Growth and Transfer of Graphene to Arbitrary Substrates. Graphene was grown in a hot-wall chemical vapor deposition (CVD) system at 1000 °C for 30 min on a copper substrate (Alfa Aesar 13382).[44] The copper substrate was positioned in the center of the furnace and supported by a quartz plate. The CVD reactor was brought to temperature over 60 min and then maintained for 30 min of annealing under 25 sccm of hydrogen. At the completion of the annealing step, the hydrogen flow was reduced to 7 sccm and methane flow initiated at 35 sccm. Following the 30 min graphene growth step, the furnace was cooled at 10 °C/min to room temperature under the methane/hydrogen flow.

A heat transfer tape (HTT) method was employed to transfer graphene to the desired substrates.[12] The HTT (REVALPHA 3195M) was applied to the copper/graphene material under 50 psi pressure using a stamp-transfer method. The HTT-supported copper/graphene material was then etched in a 0.1 M ammonium persulfate etchant bath for 24 h to remove the copper growth substrate. The resulting HTT-supported graphene was washed three times in a deionized water bath and dried in a nitrogen flow. The HTT/graphene was applied to a clean (sonicated/washed in isopropyl alcohol) substrate using the same 50 psi stamp-transfer process. The substrate/graphene/HTT material was then heated to 120 °C to release the HTT from the graphene, thus transferring the graphene to the preferred substrate.

Raman Spectroscopy. Micro-Raman (spatially resolved) spectra and maps (see Supporting Information) were taken with a Witec Alpha 300R mapping Raman system using a 532 nm laser. All maps were acquired at 100× magnification with a 600 groove/mm grating. The broad spectrum taken using this grating configuration allows for internal referencing of the 520.1 cm^{-1} peak of the silicon (100 nm thermal oxide) wafer to which the sample was transferred. Macro-Raman (nonspatially resolved) spectra were recorded in backscattering geometry using 532 nm excitation source (doubled Nd:YAG). The excitation power was 110 mW, with a spot size of ∼250 μm (∼400 W/cm^2). The CCD detector was calibrated to atomic emission lines from Oriel spectral calibration lamps.

Doping. Doping was performed by immersion of graphene TCs into the dopant solution of choice. Hydrazine doping was performed in a helium glovebox (O_2 concentration ∼0.1 ppm). Immersion for 2 h in hydrazine solutions with concentrations between 1 and 2 M, in methanol, was sufficient to reach electron concentrations of >1 × 10^{13} cm^{-2}. Nitric acid doping was performed in air. For 1L graphene TCs, immersion directly in

1−2 M nitric acid sometimes led to delamination of the graphene monolayer. To avoid this delamination, we first immersed the graphene TC in water and added concentrated nitric acid with a pipet to reach a final concentration of 1−2 M. Immersion in this 1−2 M nitric acid solution for 2 h was sufficient to reach hole concentrations of $>1 \times 10^{13}$ cm^{-2}. PEI doping was achieved by immersion in a 25% PEI (600 kDa molecular weight) solution overnight in methanol in the glovebox. Following PEI doping, the sample was dipped in methanol for a few seconds to remove excess PEI before measurements.

X-ray Photoelectron Spectroscopy. X-ray photoelectron spectra were acquired using a Physical Electronics model 5600 spectrometer and monochromatic Al Kα radiation. The electron takeoff angle was nominally 45°, and the instrument lens setting was the angle-integrating "minimum area" mode. The spectrometer binding energy scale was calibrated according to the method of Powell.[45] Wide range survey spectra were taken using a pass energy of 187.9 eV and a dwell time of 0.34 s/point, and higher resolution spectra of individual core levels were taken using a pass energy of 11.75 eV and a dwell time of 2 s/point. The "annealed" film was first measured after annealing in the UHV chamber at 450 °C for 1 h. This annealed sample was then doped with hydrazine in a separate glovebox, sealed into an air-free sample holder, and transferred without air exposure to the glovebox attached to the XPS system for measurement. Peak fitting was accomplished using the sum version of the Voigt approximation with an 80:20 Gaussian/Lorentzian mixing ratio.[46]

Hall Effect Measurements. For Hall effect measurements, graphene samples were transferred to 1 × 1 cm glass substrates. Small indium pads were pressed onto the corners of samples to make good electrical contact. Room temperature and temperature-dependent sheet resistance, mobility, Hall coefficient, and carrier density were measured on an Accent Optical Hall system equipped with a liquid nitrogen cryostat and heater. Temperature-dependent resistance measurements were conducted between 100 and 350 K in vacuum. First, the sample chamber was evacuated to a base pressure of 0.5 Torr. Then, the sample was cooled to 100 K, where the first measurement was taken. Measurements were then taken at temperature intervals of ∼15 K until the sample reached 350 K.

Absorbance Spectroscopy. Transmittance was measured on a Cary 500 UV−vis−IR spectrometer. A blank glass slide was measured as the background for all transmittance measurements, so that the displayed transmittance spectra represent the transmittance through only the graphene layers. For reference, the transmittance of a blank glass slide is ∼93% at 550 nm.

Field Effect Transistors. Bottom-gated and bottom-contacted field effect transistors were fabricated on degenerately doped silicon substrates with 100 nm thermal oxide as the gate dielectric. Source and drain contacts were evaporated gold pads, and the width of the FET channel was 2 mm. The FET channel lengths (distance between source and drain electrodes) ranged from 10 to 50 μm. The source−drain voltage for all scans shown in this study was 0.030 V.

Conflict of Interest: The authors declare no competing financial interest.

Acknowledgment. We gratefully acknowledge NREL's Laboratory Directed Research and Development (LDRD) program for funding. We thank Kevin Mistry for helpful discussions regarding n-type doping.

Supporting Information Available: Mapping Raman spectroscopy, XPS analysis of annealing of as-transferred graphene, p-type and n-type FET measurements. This material is available free of charge *via* the Internet at http://pubs.acs.org.

Note Added after ASAP Publication. This manuscript published ASAP on July 24, 2013. Due to a production error, the SI file was replaced and the correct version was reposted on August 2, 2013.

REFERENCES AND NOTES

1. Barnes, T. M.; Blackburn, J. L. Carbon Nanotube Transparent Electrodes. In *Transparent Electronics*; John Wiley & Sons, Ltd: New York, 2010; pp 185−211.
2. Minami, T. New n-Type Transparent Conducting Oxides. *MRS Bull.* **2000**, *25*, 38–44.
3. Liu, H.; Avrutin, V.; Izyumskaya, N.; Özgür, U.; Morkoç, H. Transparent Conducting Oxides for Electrode Applications in Light Emitting and Absorbing Devices. *Superlattices Microstruct.* **2010**, *48*, 458–484.
4. Chattopadhyay, D.; Queisser, H. J. Electron Scattering by Ionized Impurities in Semiconductors. *Rev. Mod. Phys.* **1981**, *53*, 745–768.
5. Barnes, T. M.; Reese, M. O.; Bergeson, J. D.; Larsen, B. A.; Blackburn, J. L.; Beard, M. C.; Bult, J.; van de Lagemaat, J. Comparing the Fundamental Physics and Device Performance of Transparent, Conductive Nanostructured Networks with Conventional Transparent Conducting Oxides. *Adv. Energy Mater.* **2012**, *2*, 353–360.
6. Blackburn, J. L.; Barnes, T. M.; Beard, M. C.; Kim, Y.-H.; Tenent, R. C.; McDonald, T. J.; To, B.; Coutts, T. J.; Heben, M. J. Transparent Conductive Single-Walled Carbon Nanotube Networks with Precisely Tunable Ratios of Semiconducting and Metallic Nanotubes. *ACS Nano* **2008**, *2*, 1266–1274.
7. Mistry, K. S.; Larsen, B. A.; Bergeson, J. D.; Barnes, T. M.; Teeter, G.; Engtrakul, C.; Blackburn, J. L. n-Type Transparent Conducting Films of Small Molecule and Polymer Amine Doped Single-Walled Carbon Nanotubes. *ACS Nano* **2011**, *5*, 3714–3723.
8. Tenent, R. C.; Barnes, T. M.; Bergeson, J. D.; Ferguson, A. J.; To, B.; Gedvilas, L. M.; Heben, M. J.; Blackburn, J. L. Ultrasmooth, Large-Area, High-Uniformity, Conductive Transparent Single-Walled-Carbon-Nanotube Films for Photovoltaics Produced by Ultrasonic Spraying. *Adv. Mater.* **2009**, *21*, 3210–3216.
9. Vosgueritchian, M.; Lipomi, D. J.; Bao, Z. Highly Conductive and Transparent PEDOT:PSS Films with a Fluorosurfactant for Stretchable and Flexible Transparent Electrodes. *Adv. Funct. Mater.* **2012**, *22*, 421–428.
10. Lee, J.-Y.; Connor, S. T.; Cui, Y.; Peumans, P. Solution-Processed Metal Nanowire Mesh Transparent Electrodes. *Nano Lett.* **2008**, *8*, 689–692.
11. Hu, L.; Kim, H. S.; Lee, J.-Y.; Peumans, P.; Cui, Y. Scalable Coating and Properties of Transparent, Flexible, Silver Nanowire Electrodes. *ACS Nano* **2010**, *4*, 2955–2963.
12. Bae, S.; Kim, H.; Lee, Y.; Xu, X.; Park, J.-S.; Zheng, Y.; Balakrishnan, J.; Lei, T.; Ri Kim, H.; Song, Y. I.; *et al.* Roll-to-Roll Production of 30-Inch Graphene Films for Transparent Electrodes. *Nat. Nanotechnol.* **2010**, *5*, 574–578.
13. Kholmanov, I. N.; Magnuson, C. W.; Aliev, A. E.; Li, H.; Zhang, B.; Suk, J. W.; Zhang, L. L.; Peng, E.; Mousavi, S. H.; Khanikaev, A. B.; *et al.* Improved Electrical Conductivity of Graphene Films Integrated with Metal Nanowires. *Nano Lett.* **2012**, *12*, 5679–5683.
14. Li, X.; Cai, W.; An, J.; Kim, S.; Nah, J.; Yang, D.; Piner, R.; Velamakanni, A.; Jung, I.; Tutuc, E.; *et al.* Large-Area Synthesis of High-Quality and Uniform Graphene Films on Copper Foils. *Science* **2009**, *324*, 1312–1314.
15. Ni, G.-X.; Zheng, Y.; Bae, S.; Tan, C. Y.; Kahya, O.; Wu, J.; Hong, B. H.; Yao, K.; Özyilmaz, B. Graphene-Ferroelectric Hybrid Structure for Flexible Transparent Electrodes. *ACS Nano* **2012**, *6*, 3935–3942.
16. Jeong, C.; Nair, P.; Khan, M.; Lundstrom, M.; Alam, M. A. Prospects for Nanowire-Doped Polycrystalline Graphene Films for Ultratransparent, Highly Conductive Electrodes. *Nano Lett.* **2011**, *11*, 5020–5025.
17. Kim, K. S.; Zhao, Y.; Jang, H.; Lee, S. Y.; Kim, J. M.; Kim, K. S.; Ahn, J.-H.; Kim, P.; Choi, J.-Y.; Hong, B. H. Large-Scale Pattern Growth of Graphene Films for Stretchable Transparent Electrodes. *Nature* **2009**, *457*, 706–710.
18. Shi, Y.; Kim, K. K.; Reina, A.; Hofmann, M.; Li, L.-J.; Kong, J. Work Function Engineering of Graphene Electrode *via* Chemical Doping. *ACS Nano* **2010**, *4*, 2689–2694.
19. Lee, Y.-Y.; Tu, K.-H.; Yu, C.-C.; Li, S.-S.; Hwang, J.-Y.; Lin, C.-C.; Chen, K.-H.; Chen, L.-C.; Chen, H.-L.; Chen, C.-W. Top Laminated Graphene Electrode in a Semitransparent Polymer Solar Cell by Simultaneous Thermal Annealing/Releasing Method. *ACS Nano* **2011**, *5*, 6564–6570.

20. Nair, R. R.; Blake, P.; Grigorenko, A. N.; Novoselov, K. S.; Booth, T. J.; Stauber, T.; Peres, N. M. R.; Geim, A. K. Fine Structure Constant Defines Visual Transparency of Graphene. *Science* **2008**, *320*, 1308.
21. Kasry, A.; Kuroda, M. A.; Martyna, G. J.; Tulevski, G. S.; Bol, A. A. Chemical Doping of Large-Area Stacked Graphene Films for Use as Transparent, Conducting Electrodes. *ACS Nano* **2010**, *4*, 3839–3844.
22. Suk, J. W.; Lee, W. H.; Lee, J.; Chou, H.; Piner, R. D.; Hao, Y.; Akinwande, D.; Ruoff, R. S. Enhancement of the Electrical Properties of Graphene Grown by Chemical Vapor Deposition *via* Controlling the Effects of Polymer Residue. *Nano Lett.* **2013**, *13*, 1462–1467.
23. Yan, H.; Xia, F.; Zhu, W.; Freitag, M.; Dimitrakopoulos, C.; Bol, A. A.; Tulevski, G.; Avouris, P. Infrared Spectroscopy of Wafer-Scale Graphene. *ACS Nano* **2011**, *5*, 9854–9860.
24. Wei, P.; Liu, N.; Lee, H. R.; Adijanto, E.; Ci, L.; Naab, B. D.; Zhong, J. Q.; Park, J.; Chen, W.; Cui, Y.; *et al.* Tuning the Dirac Point in CVD-Grown Graphene through Solution Processed n-Type Doping with 2-(2-Methoxyphenyl)-1,3-dimethyl-2,3-dihydro-1*H*-Benzoimidazole. *Nano Lett.* **2013**, *13*, 1890–1897.
25. Das, A.; Pisana, S.; Chakraborty, B.; Piscanec, S.; Saha, S. K.; Waghmare, U. V.; Novoselov, K. S.; Krishnamurthy, H. R.; Geim, A. K.; Ferrari, A. C.; *et al.* Monitoring Dopants by Raman Scattering in an Electrochemically Top-Gated Graphene Transistor. *Nat. Nanotechnol.* **2008**, *3*, 210–215.
26. Cançado, L. G.; Jorio, A.; Ferreira, E. H. M.; Stavale, F.; Achete, C. A.; Capaz, R. B.; Moutinho, M. V. O.; Lombardo, A.; Kulmala, T. S.; Ferrari, A. C. Quantifying Defects in Graphene *via* Raman Spectroscopy at Different Excitation Energies. *Nano Lett.* **2011**, *11*, 3190–3196.
27. Das, A.; Chakraborty, B.; Sood, A. K. Raman Spectroscopy of Graphene on Different Substrates and Influence of Defects. *Bull. Mater. Sci.* **2008**, *31*, 579–584.
28. Ramanathan, T.; Fisher, F. T.; Ruoff, R. S.; Brinson, L. C. Amino-Functionalized Carbon Nanotubes for Binding to Polymers and Biological Systems. *Chem. Mater.* **2005**, *17*, 1290–1295.
29. Chen, J. H.; Jang, C.; Adam, S.; Fuhrer, M. S.; Williams, E. D.; Ishigami, M. Charged-Impurity Scattering in Graphene. *Nat. Phys.* **2008**, *4*, 377–381.
30. Ponomarenko, L. A.; Yang, R.; Mohiuddin, T. M.; Katsnelson, M. I.; Novoselov, K. S.; Morozov, S. V.; Zhukov, A. A.; Schedin, F.; Hill, E. W.; Geim, A. K. Effect of a High-kappa Environment on Charge Carrier Mobility in Graphene. *Phys. Rev. Lett.* **2009**, *102*, 206603.
31. Schedin, F.; Geim, A. K.; Morozov, S. V.; Hill, E. W.; Blake, P.; Katsnelson, M. I.; Novoselov, K. S. Detection of Individual Gas Molecules Adsorbed on Graphene. *Nat. Mater.* **2007**, *6*, 652–655.
32. Cheng, Z.; Zhou, Q.; Wang, C.; Li, Q.; Wang, C.; Fang, Y. Toward Intrinsic Graphene Surfaces: A Systematic Study on Thermal Annealing and Wet-Chemical Treatment of SiO_2-Supported Graphene Devices. *Nano Lett.* **2011**, *11*, 767–771.
33. Fratini, S.; Guinea, F. Substrate-Limited Electron Dynamics in Graphene. *Phys. Rev. B* **2008**, *77*, 195415.
34. Yan, R.; Zhang, Q.; Li, W.; Calizo, I.; Shen, T.; Richter, C. A.; Hight-Walker, A. R.; Liang, X.; Seabaugh, A.; Jena, D.; *et al.* Determination of Graphene Work Function and Graphene-Insulator-Semiconductor Band Alignment by Internal Photoemission Spectroscopy. *Appl. Phys. Lett.* **2012**, *101*, 022105.
35. Gomez De Arco, L.; Zhang, Y.; Schlenker, C. W.; Ryu, K.; Thompson, M. E.; Zhou, C. Continuous, Highly Flexible, and Transparent Graphene Films by Chemical Vapor Deposition for Organic Photovoltaics. *ACS Nano* **2010**, *4*, 2865–2873.
36. Jo, G.; Na, S.-I.; Oh, S.-H.; Lee, S.; Kim, T.-S.; Wang, G.; Choe, M.; Park, W.; Yoon, J.; Kim, D.-Y.; *et al.* Tuning of a Graphene-Electrode Work Function To Enhance the Efficiency of Organic Bulk Heterojunction Photovoltaic Cells with an Inverted Structure. *Appl. Phys. Lett.* **2010**, *97*, 213301–213303.
37. Reese, M. O.; White, M. S.; Rumbles, G.; Ginley, D. S.; Shaheen, S. E. Optimal Negative Electrodes for Poly(3-hexylthiophene): [6,6]-Phenyl C61-Butyric Acid Methyl Ester Bulk Heterojunction Photovoltaic Devices. *Appl. Phys. Lett.* **2008**, *92*, 053307–053303.
38. Chen, J.-H.; Jang, C.; Xiao, S.; Ishigami, M.; Fuhrer, M. S. Intrinsic and Extrinsic Performance Limits of Graphene Devices on SiO_2. *Nat. Nanotechnol.* **2008**, *3*, 206–209.
39. Zhu, W.; Perebeinos, V.; Freitag, M.; Avouris, P. Carrier Scattering, Mobilities, and Electrostatic Potential in Monolayer, Bilayer, and Trilayer Graphene. *Phys. Rev. B* **2009**, *80*, 235402.
40. Li, Q.; Hwang, E. H.; Das Sarma, S. Disorder-Induced Temperature-Dependent Transport in Graphene: Puddles, Impurities, Activation, and Diffusion. *Phys. Rev. B* **2011**, *84*, 115442.
41. Barnes, T. M.; Blackburn, J. L.; van de Lagemaat, J.; Coutts, T. J.; Heben, M. J. Reversibility, Dopant Desorption, and Tunneling in the Temperature-Dependent Conductivity of Type-Separated, Conductive Carbon Nanotube Networks. *ACS Nano* **2008**, *2*, 1968–1976.
42. Ameri, T.; Li, N.; Brabec, C. J. Highly Efficient Organic Tandem Solar Cells: A Follow up Review. *Energy Environ. Sci.* **2013**, *6*, 2390–2413.
43. Chandra, B.; Afzali, A.; Khare, N.; El-Ashry, M. M.; Tulevski, G. S. Stable Charge-Transfer Doping of Transparent Single-Walled Carbon Nanotube Films. *Chem. Mater.* **2010**, *22*, 5179–5183.
44. Li, X.; Zhu, Y.; Cai, W.; Borysiak, M.; Han, B.; Chen, D.; Piner, R. D.; Colombo, L.; Ruoff, R. S. Transfer of Large-Area Graphene Films for High-Performance Transparent Conductive Electrodes. *Nano Lett.* **2009**, *9*, 4359–4363.
45. Powell, C. J. Energy Calibration of X-ray Photoelectron Spectrometers: Results of an Interlaboratory Comparison to Evaluate a Proposed Calibration Procedure. *Surf. Interface Anal.* **1995**, *23*, 121–132.
46. Hesse, R.; Streubel, P.; Szargan, R. Product or Sum: Comparative Tests of Voigt, and Product or Sum of Gaussian and Lorentzian Functions in the Fitting of Synthetic Voigt-Based X-ray Photoelectron Spectra. *Surf. Interface Anal.* **2007**, *39*, 381–391.